Formation of conical fractures in sedimentary basins: experiments involving pore fluids and implications for sandstone intrusion mechanisms

Régis Mourgues, Denis Bureau, Ludovic Bodet, Aurélien Gay, Jean Baptiste Gressier

Formation of conical fractures in sedimentary basins: Experiments involving pore fluids and implications for sandstone intrusion mechanisms

R. Mourgues [a,*], D. Bureau [a], L. Bodet [c], A. Gay [b], J.B. Gressier [a]

[a] L.P.G.N., CNRS UMR 6112, University of Maine, Faculty of Sciences, 72085 Le Mans, France
[b] Géosciences Montpellier, CNRS UMR 5243, 34095 Montpellier cedex 5, France
[c] CNRS UMR 7619 Sisyphe, University Pierre et Marie Curie-Paris 6, France

Large sand intrusions often exhibit conical morphologies analogous to magmatic intrusions such as saucer-shaped or cup-shaped sills. Whereas some physical processes may be similar, we show with scaled experiments that the formation of conical sand intrusions may be favoured by the pore-pressure gradients prevailing in the host rock before sand injection. Our experiments involve injecting air into a permeable and cohesive analogue material to produce hydraulic fractures while controlling the pore pressure field. We control the state of overpressure in the overburden by applying homogeneous basal pore pressure, and then adding a second local pore pressure field by injecting air via a central injector to initiate hydraulic fractures near the injection point. In experiments involving small vertical effective stresses (small overburden, or high pore fluid overpressure), the fracturing pressure (λ_{fract}) is supralithostatic and two dipping fractures are initiated at the injection point forming a conical structure. From theoretical considerations, we predict that high values of λ_{fract} are due to strong cohesion or high pore fluid overpressure distributed in the overburden. Such conditions are favoured by the pore pressure/stress coupling induced by both pore pressure fields. The dips of cones can be accounted for elastic-stress rotation occurring around the source. Contrary to magmatic chamber models, the aqueous fluid overpressure developed in a parent sandbody (and prevailing before the formation of injectites) may diffuse into the surrounding overburden, thus favouring stress rotation and the formation of inclined sheets far from the parent source. For experiments involving higher vertical effective stresses (thick overburden or low pore fluid overpressure), the fracturing pressure is lower than the lithostatic stress, and a single fracture is opened in mode I which then grows vertically. At a critical depth, the fracture separates into two dilatant branches forming a flat cone. We make use of a P.I.V. (Particle Imaging Velocimetry) technique to analyse plastic deformation, showing that these inclined fractures are opened in mixed modes. Close to the surface, they change into steep shear bands where fluids can infiltrate. The final morphology of the fracture network is very similar to the common tripartite architecture of various injection complexes, indicating that different mechanisms may be involved in the formation of dykes. Feeder dykes under the sill zones may open as tensile fractures, while overlying dykes may be guided by the deformation induced by the growth of sills. These deformation conditions may also favour the formation of fluid escape structures and pockmarks.

1. Introduction

Seismic and outcrop studies have led to the recognition of shallow-level sandstone and magmatic intrusions in sedimentary basins that have similar cone-, saucer- and cup-shaped geometries (sandstone: Cartwright, 2007, 2010; Davies, 2003; Huuse and Mickelson, 2004; Surlyk et al., 2007; Vigorito and Hurst, 2010; Vigorito et al., 2008; magmatic: Goulty and Schofield, 2008; Polteau et al., 2008; Thompson and Schofield, 2008). Until recently, sandstone intrusions were not generally considered as having any economic significance. But the wider availability of 3D seismic and high-resolution well logging data has led to the increasing identification of sandstone intrusions acting as reservoirs or fluid migration pathways (Hurst and Cartwright, 2007; Hurst et al., 2003; Jenkins, 1930) in a number of petroliferous sedimentary basins, thus highlighting the need to improve our understanding of their genesis (De Boer et al., 2007; Duranti et al., 2002; Huuse and Mickelson, 2004; Huuse et al., 2005; Schwartz et al., 2003).

The similar geometries observed in magmatic and sand intrusions imply that emplacement mechanisms are likely controlled by common physical parameters (Cartwright et al., 2008; Polteau et al., 2008). For example, saucer-shaped intrusions in magmatic and sandstone settings exhibit similar geometries (Hansen and Cartwright, 2006a, b; Malthe-Sorenssen et al., 2004; Polteau et al., 2008; Thomson and Hutton, 2004): a subhorizontal sill at the base, a steeply dipping

* Corresponding author. Tel.: +33 243833237.
E-mail address: Regis.Mourgues@univ-lemans.fr (R. Mourgues).

inclined sheet cross-cutting the stratification, and a sub-horizontal outer-sill. This shape seems to arise from the interaction between the horizontally propagating shallow hydraulic fracture filled with low-viscosity fluid and deformation in the overburden (Fig. 1a) (Galland et al., 2009; Goulty and Schofield, 2008; Malthe-Sorenssen et al., 2004; Pollard and Johnson, 1973). The horizontal inflating fracture propagates until it reaches a critical length. Beyond this value, the deformed free surface induces the development of an asymmetrical stress field and a non-zero value for the mode II stress intensity factor, thus favouring the upward deflection of the sill tips and the formation of inclined margins. This model, first described by Pollard and Johnson (1973), has been supported by more recent formulations (Fialko et al., 2001) and the formation of artificial hydraulic fractures (Murdoch, 2002; Murdoch and Slack, 2002), as well as the development of numerical models (Malthe-Sorenssen et al., 2004) and analogue models (Galland et al., 2009). The ratio between inner sill diameter and emplacement depth (W/D) varies from 1.5 in experimental studies (Galland et al., 2009) to 4–5 (Polteau et al., 2008) for the emplacement of sills in stratified basins. Indeed, low-strength layers may favour horizontal propagation of sills and higher W/D ratios. While flat based bowl-shaped sandstone intrusions in sedimentary basins exhibit similar morphologies to magmatic intrusions, Cartwright et al. (2008) measured lower W/D ratios ranging only between 0.7 and 1.1. These low ratios are not only due to post-emplacement compaction, but also indicate the more pronounced tendency of clastic sills to develop inclined sheets. Conical sandstone intrusions with well-defined apices are very common in basins such as the North Sea and Faroes–Shetland basins (Cartwright et al., 2008; Huuse and Mickelson, 2004; Shoulders and Cartwright, 2004; Shoulders et al., 2007). As regards saucer-shaped intrusion, the formation of cones is associated with an uplift of the free surface and the formation of a forced fold (Fig. 1b) (Cartwright et al., 2008; Galland et al., 2009; Hansen and Cartwright, 2006b; Malthe-Sorenssen et al., 2004; Pollard and Holzhausen, 1979). The mechanical explanation for saucer-shaped magmatic sills cannot be applied to this class of intrusions. Nevertheless, their morphological analogy with certain magmatic cone sheets led Cartwright et al. (2008) to conclude that similar emplacement mechanisms were involved in their formation. Magmatic cones are inward-dipping sheet intrusions that are emplaced above a central magmatic complex. The inclination of the sheets, assumed to open in mode I, is attributed to the stress distribution around the magma chamber, which is modelled as a nucleus of strain (Anderson, 1936; Mogi, 1958) or as a fluid-filled cavity (Gudmundson, 2006; Gudmundsson, 1990). In such models, the stress trajectories are largely governed by the shape of the contact between the magma chamber and the overburden. Following this idea, Cartwright et al. (2008) proposed that the formation of small cupola-shaped laccoliths of sand at the top of a feeder dyke may provide the required stress conditions for the formation of conical intrusions (Fig. 1d). An alternative explanation was inferred from analogue experiments simulating magmatic intrusions, where conical sheets were also observed in cases of dykes approaching the surface (Galland et al., 2009; Mathieu et al., 2008). Following several authors (Koide and Bhattacharji, 1975; Mastin and Pollard, 1988; Pollard, 1973) who predicted extension at the tip of an enlarging dyke, Mathieu et al. (2008) proposed that magmatic fluids of low viscosity are channelled by faults that develop at the tip of a vertical dyke, thus forming a cone (Fig. 1c).

Recent detailed observations on the Panoche Giant Complex, the best exposed known outcrop representing an analogue of regionally developed sand intrusions (Vigorito and Hurst, 2010; Vigorito et al., 2008), have yielded a detailed description of the complex features of sand injectites. Vigorito and Hurst (2010) defined a tripartite architecture of the injection complex, with an intrusive sill zone occurring in a restricted stratigraphic interval, vertically bounded by two zones of high-angle dykes. The sill zone is characterized by subhorizontal sills and large low angle dykes (<30°) cross-cutting up to 230 m of host strata. The low-angle dykes in this zone have random strike distributions and could be regarded as structures equivalent to giant cones or bowl-shaped intrusions defined from seismic data. The clastic dykes observed above and below the sill zone have well defined strike directions. Such dykes may be important pathways for fluid migration, but they are difficult to identify on seismic profiles because of their steepness. This tripartite architecture has been also recognized in other injectite complexes (e.g. north coast of Santa Cruz (USA), New Madrid (USA)).

Although there may be numerous similarities between magmatic hydraulic fracturing processes and hydrofracturing involved in sand injection, some physical aspects are substantially different as

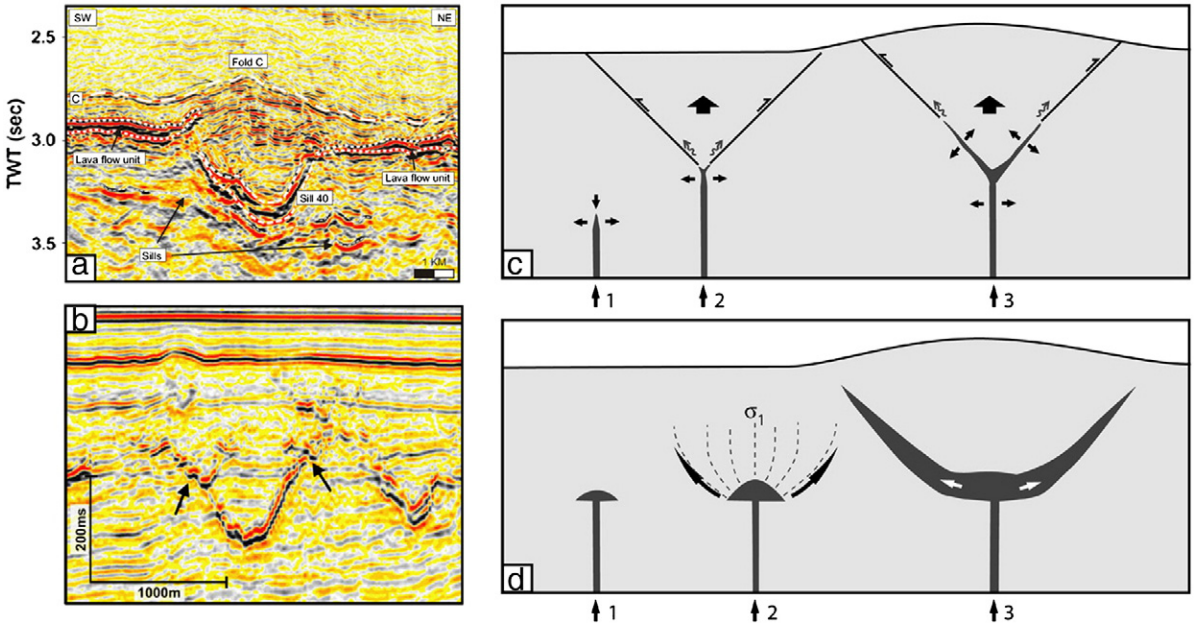

Fig. 1. a–b: Similar morphologies are observed in magmatic saucer-shaped intrusions (a) after Hansen and Cartwright(2006b) and in V-shaped sand intrusions (b) after Cartwright et al.(2008)). c–d: Distinct hypotheses for formation of conical structures. c: According to Mathieu et al. (2008), a low-viscosity fluid percolates in conjugate faults developing at the tip of a vertical feeder dyke. d: According to Cartwright et al. (2008), a small laccolith of sand forms at the top of a feeder dyke. The cupola-shape provides the required σ_1 rotation allowing the development of inclined sheets.

suggested by Rodrigues et al. (2009). For igneous intrusions, magma can migrate no more than a short distance through sedimentary pores and the fluid pressure remains confined within the intrusive body. By contrast, fluids responsible for the formation of sand injectites are aqueous and can percolate through the pores over a greater distance, thus modifying the effective stress field in the vicinity of the structure. Indeed, according to the principle of effective stresses, the pore fluid reduces the stresses and, consequently, also diminishes the apparent strength of the overburden. Moreover, the seepage forces induced by the non-vertical pore fluid overpressure gradient may lead to rotation of the stress tensor (Mourgues and Cobbold, 2003), possibly favouring the formation of inclined hydrofractures and cones.

To understand the effects of pore fluid overpressure on the formation of vertical conduits and conical structures, we conducted new analogue hydrofracturing experiments. By comparing our results with analytical and numerical predictions, we show that a pore pressure field around a parent sandbody or distributed in the overburden favours the formation of inclined sheets. Finally, the use of P.I.V. (Particle Imaging Velocimetry) allows us to image the deformation occurring during cone growth, thus providing some mechanical explanations for the formation of tripartite architectures in injectite complexes

2. Experimental set-up and scaling

The formation of sandstone intrusions requires several successive processes: pressure build-up in a parent sandbody, hydrofracturing of the overburden, and then fluidized flow of sand/fluid mixture into the fracture. The aim of our physical experiments was not to model injectites following the approach of Rodrigues et al. (2009), but to improve our understanding of the role of pore pressure in shallow hydraulic fracturing and the formation of conical structures. Consequently, we conducted hydraulic fracturing experiments using constrained pore pressure fields without attempting to model the fluidization and sand injection processes.

2.1. Scaling: solid materials and pore fluid

Hydraulic fracturing was previously studied with various fracturing fluids and solid materials (Galland et al., 2009; Hubbert and Willis, 1957; Kavanagh et al., 2006; Mastin and Pollard, 1988; Menand, 2008; Murdoch, 1992; Takada, 1990). Many experiments were carried out with elastic gelatine fractured by water to simulate the propagation of magmatic dykes and sills or to validate the predictions of fracture shape and growth in elastic media (Galland et al., 2009; Kavanagh et al., 2006; Menand, 2008; Takada, 1990). Gelatine is an impermeable material that fails under tension, but it is too cohesive to allow plastic shearing. To overcome this difficulty, several authors have used granular cohesive materials to simulate magmatic fracturing (Chang, 2004; Galland et al., 2009; Mathieu et al., 2008). Galland et al. (2009) injected vegetable oil into cohesive silica powder to simulate sills and saucer-shaped sill emplacement, while Mathieu et al. (2008) injected low-viscosity honey into ignimbrite powder. Hydraulic fracturing around a borehole was simulated by injecting joint compound into silica powder and dry clays (Chang, 2004). All these experiments and materials are well suited to simulate external hydraulic fracturing processes (Price and Cosgrove, 1990) where the fluid does not percolate into the overburden without fracturing (magmatic processes, fractures around boreholes). Nevertheless, this approach cannot be used to simulate hydraulic fractures induced by water in water-saturated sediments because, under such conditions, the aqueous fracturing fluid already fills all available pores in the overburden. This pore fluid may modify the effective stresses in the solid framework and modify the fracturing process. Cobbold and Castro first used models with pore fluids in a sandbox, and demonstrated that the injection of air can simulate (Cobbold and Castro, 1999) the mechanical effect of pore fluid overpressure (pore pressure higher than the hydrostatic pressure). Mourgues and Cobbold (2003, 2006a,b) and Mourgues et al. (2009) experimentally investigated the consequences of pore fluid overpressure on the formation of listric faults (Mourgues and Cobbold, 2003), on the development of accretionary wedges (Mourgues and Cobbold, 2006b) and on the triggering of gravitational instabilities in sedimentary deltas (Mourgues and Cobbold, 2006a; Mourgues et al., 2009). Since all these experiments used non-cohesive sand, similar types of model cannot be used to simulate tensile failure and hydraulic fracture. Recently, Rodrigues et al.(2009) combined the technique of air injection developed by Mourgues and Cobbold (2006b) and various cohesive and non-cohesive materials to simulate the formation of clastic intrusions. They used microballs to simulate the intruding sandy material and silica powder for the cohesive sealing formation. A similar approach was followed by Gressier et al. (2010), who injected silicone into diatomite powder subjected to vertical air pore-pressure gradients to study the effect of pore-overpressure on the dyke-to-sill transition depth.

As the aim of our experimental study was to understand how the pore pressure field influences the formation of conical fractures, we chose to use diatomite powder to simulate the brittle sedimentary cover. In contrast, diatomite has a non-negligible permeability varying between 1 and 15 darcy, depending on compaction. In our experiments, the measured permeability of the powder was 6 darcy for a density of 300 kg/m^3. This value is high enough to ensure reliable control of the pore-pressure field in the model. Like silica powder, diatomite powder is sufficiently cohesive to allow tensile failure. The yield stress was measured by Mourgues et al. (2011) with shear tests. For small effective stresses, a powder of 300 kg/m^3 of density exhibited a Griffith's envelope with a measured tensile strength of 80 Pa. This value was confirmed by horizontal hydraulic fracturing tests (Mourgues et al., 2011).

The scaling procedure, based on the standard similarity conditions (Hubbert, 1937; Ramberg, 1981), defines dimensionless numbers that characterize the kinematics and kinetics of the simulated processes. Using these numbers, we define the scaling ratios (Table 1). From the equilibrium equation of effective stresses and pore pressure (Mourgues and Cobbold, 2003), we derive two dimensionless numbers:

$$\pi_1 = \sigma_o/(\rho_o g_o L_o) \quad (1)$$

$$\pi_2 = P_o/(\rho_o g_o L_o) \quad (2)$$

Table 1
Experimental variables and their values in experiments compared with standard natural values. The effective density of host rock is corrected from the buoyancy force.

		Nature (r)	Experiment (m)	ratio
L_o	Length (m)	500	0.15	0.0003
g_o	Gravity (ms^{-2})	9.81	9.81	1
ρ_o	Effective density of host rock (kg/m^3)	1250	300	0.24
σ_o	Gravitational stresses (Pa)	6,131,250	441.45	0.000072
p_o	Pore fluid overpressure ($\lambda = 1$) (Pa)	6,131,250	441.45	0.000072
ϕ	Angle of internal friction	30	30	1
T_o	Tensile strength (Pa)	1.10E+06	80	7.27E−05
ν	Poisson's ratio	0.2–0.4	0.35	1
E_o	Young modulus (Pa)	1.00E+08	1.00E+06	1.00E−02
k_o	Permeability of country rock (m^{-2})	1.00E−18	8.00E−12	8.00E+06
η_o	Fluid viscosity (Pa.s)	1.00E−03	1.80E−05	1.80E−02
χ_o	Specific storage (Pa^{-1})	1.20E−08	9.20E−06	7.67E+02
t_o	Diffusion time on L_o (s)	3.00E+12	4.60E−01	1.53E−13
Re	Reynolds number	1000–>100,000	10–>200	

where σ_o, P_o, ρ_o, g_o, L_o are, respectively, stress, pore fluid overpressure, the effective density ($(1-\phi_p)(\rho_s-\rho_w)$) corrected from buoyancy effect, the acceleration due to gravity and the characteristic length of the system (ϕ_p is the porosity). These dimensionless numbers express the ratio between surface and gravity forces (Ramberg, 1981). They must have similar values in nature and experiments, so we obtain:

$$\gamma_\sigma = \frac{\sigma_m}{\sigma_r} = \frac{L_m}{L_r}\frac{\rho_m}{\rho_r}\frac{g_m}{g_r} = \frac{P_m}{P_r} = \gamma_P \tag{3}$$

where γ is the scaling ratio. Subscript m refers to values in the experiment and r to values in nature. From Eq. (3), we can see that scaling ratios for stresses and pore fluid overpressure are similar. If we consider a 15-cm thick model made of diatomite as representing a mean depth of 500 m for the formation of conical intrusions (Cartwright et al., 2008; Polteau et al., 2008; Shoulders and Cartwright, 2004), the stress ratio is $7.2*10^{-5}$ (Table 1). Pore-fluid pressure in the model and in the field can be characterized by the dimensionless ratio (Davis et al., 1983):

$$\lambda^* = P_{ov}/\rho g z \tag{4}$$

where P_{ov} is the fluid overpressure (non-hydrostatic part of the pore-fluid pressure) and ρ the effective density (corrected from buoyancy). The scaling of the fracturing pore-pressure requires a correct scaling of the brittle behaviour of sediments. The failure envelope is determined by the Mohr–Coulomb criterion for shear failure and by the Griffith criterion for extensional failure (Jaeger and Cook, 1969). The first dimensionless number corresponds to the angle of internal friction ϕ:

$$\pi_3 = \phi \tag{5}$$

ϕ is estimated as 31° for diatomite powder, which is within the range of values for sediments. The second dimensionless number is the ratio between tensile strength T (or cohesion ($C=2T$ according to Griffith's law)) and gravitational forces:

$$\pi_4 = T_o/(\rho_o g_o L_o). \tag{6}$$

From π_4 and Eq. (4), we infer that $\gamma_T=\gamma_\sigma$. Assuming a stress ratio of $7.2*10^{-5}$, a tensile strength of 80 Pa in the diatomite simulates a tensile strength of around 1.1 MPa at 500 m depth in nature, which is a reasonable value for sediments such as shale or weakly consolidated mudstone (Horsrud et al., 1998; Lothe et al., 2004).

Before failure, the elastic response of the overburden controls the coupling between effective stresses and pore-pressure variations (Mourgues et al., 2011; Rozhko et al., 2007). Consequently, elastic behaviour has to be taken into account when estimating fracture pressure. Poisson's ratio ν is the first dimensionless parameter.

$$\pi_5 = \nu \tag{7}$$

Since ν is the main elastic parameter controlling the failure pressure and pore pressure/stress coupling in a sedimentary basin (Mourgues et al., 2011), it must be appropriately scaled. In the diatomite powder, Poisson's ratio is estimated at 0.35, which is not far from typical values in weakly consolidated sediments (Lothe et al., 2004). According to the equations of linear elasticity (Jaeger and Cook, 1969), a second dimensionless number is obtained from the ratio between the stress and Young's modulus E defining elastic deformation:

$$\pi_6 = \sigma_o/E_o. \tag{8}$$

We can easily deduce that $\gamma_E=\gamma_\sigma$. Assuming Young's moduli range between 10^8 and 10^9 Pa for clay-rich sediments, the stress ratio leads to values of between 7200 and 72,000 Pa for the analogue material. For the diatomite powder, E is estimated at 10^6 Pa. Therefore, elastic deformation is not properly scaled and is consequently smaller than required by Eq. (8).

Our study aims to simulate the effect of pore-fluid overpressure on the formation of conical hydrofractures. Before failure, the pore-pressure field and the fluid migration through porous rocks are described by Darcy's law:

$$q = -k/\eta \nabla P_{ov} \tag{9}$$

where q is the Darcy velocity, η the fluid viscosity and k the intrinsic permeability of the medium. From Eq. (9), we define a new dimensionless number:

$$\pi_6 = k_o P_o/(\eta_o L_o q_o) \tag{10}$$

and a scaling ratio for the fluid flow in the overburden:

$$\gamma_q = \gamma_k \gamma_P \gamma_h{}^{-1} \gamma_L{}^{-1}. \tag{11}$$

For practical reasons, we use air as the pore fluid and derive a scaling ratio $\gamma_q \approx 10^8$. By using this ratio and suitable boundary conditions for the fluid flow, we are able to obtain the required pore pressure field, seepage forces and effective stress field within the model. Any change of the pore fluid pressure is propagated in the overburden according to the diffusivity equation:

$$dP/dt = k/(\eta S)\nabla^2 P_{ov} \tag{12}$$

where S is the specific storage, and t the time. The pore pressure diffusion time is:

$$t_o = \eta_o S_o L_o{}^2/k_o. \tag{13}$$

The diffusion time of air pressure in a 15 cm thick model is estimated at 0.4 s, and the fluid flow rapidly attains a steady state. With such a short diffusion time, we can ensure time control of the pore-pressure field prior to the initiation of hydraulic failure. In nature, this reference time corresponds to 100,000 years, which is less than the time typically required for a sandbody to be buried to 500 m. During this period, a similar steady-state pressure field may develop in the overburden surrounding a sandbody which is pressurized, for example, by lateral pressure transfer. In our experiments, the diffusion time is similar to the propagation time of the fractures through the model (0.5 s). Hence, during fracture growth, the pore-pressure field evolves dynamically and it becomes difficult to estimate its time-variation correctly. Sand injectites may build up very quickly and lead to changes in dynamic pore-pressure. As soon as a fracture opens, a Couette-type flow regime begins. In nature, the flow involves fluidized material, whereas our experiments only involve air. The flow regime is predicted by the Reynolds number Re, which is the ratio between inertial and viscous forces:

$$Re = \rho_f l_o U_o/\eta_o \tag{14}$$

where ρ_f is the fluid density, l_o is the intrusion thickness and U_o the fluid velocity in the fracture. In our experiments, we calculate Re numbers ranging from 10 to 100, which are indicative of laminar flow. In natural sand injection, fluidized flows may vary from laminar to turbulent (Duranti, 2007) depending on the viscosity of the fluidized material. Rodrigues et al. (2009) stressed the difficulty of properly scaling high Re numbers during sand injection experiments.

2.2. Apparatus

The experimental apparatus consisted of a modified Hele–Shaw cell, 1 m long and 70 cm high and 2.5 cm thick. To limit the silo effect

(Mourgues and Cobbold, 2003), which can limit the vertical stress, the walls were made of low-friction glass and the models were no thicker than 30 cm. A Janssen model (Janssen, 1895) was used to evaluate the vertical stress. Hydraulic fractures were initiated by injecting air through a central injector (Fig. 2), which was 2 mm wide. This localized injection of air created a non-homogeneous pressure field around the injector. A basal pore pressure (λ_b) was applied at the base of the model by means of a reservoir of compressed air. This second injection of air was laterally homogeneous and allowed us to modify the mean vertical effective stress.

2.3. Experimental set-up

All experiments followed the same procedure: i) powder was put into the apparatus; ii) air pressure in the central injector was increased slowly to reach the required basal pore pressure value λ_b; iii) slow increase of air flow at the injector until formation of a fracture. The failure pressure λ_b was then recorded.

The increase of pore pressure was slow enough such that it approximated to a steady state. Once a fracture formed, it grew quickly towards the top of the model in approximately 0.5 s. All experiments were filmed with a high speed CEMOS camera (100 fps).

Three series of experiments were carried out (Fig. 3), using model thicknesses of 14, 20 and 26 cm, with the central injection point located at depths of 9.5, 15 and 20 cm in models A, B and C, respectively. In each series, we conducted several experiments with various basal pore pressures λ_b varying between 0 and 1 (Fig. 3).

3. Experimental results

In series A, 15 experiments were carried out. Some of these experiments are shown in Fig. 3. In the experiments involving a very high basal distributed pore pressure ($\lambda_b = 1$) (Fig. 3A5), tensile fractures opened horizontally from the injector. In all the other experiments (exp. A1–A4), two hydraulic fractures initiated at the central injector forming a V-shaped structure. We consider that the 2D features are analogues of 3D conical fractures. Indeed, Mathieu et al. (2008) conducted experiments that could be compared to ours. These authors injected viscous fluid into silica powder and obtained 3D conical intrusions. They also conducted "half-box" experiments in which the feeder tube was placed along the glass wall of the box. While these intrusions formed partly in 3D, it was also possible to observe their growth in cross-section (2D). Our experiments are in agreement with Mathieu et al. (2008) observations along the glass wall, and we assume that our 2D "V" shapes are analogues of 3D cones. Fig. 3 clearly shows that the cones flatten with increasing basal pore pressure λ_b. For $\lambda_b = 0$, the cone is very narrow (exp. A1), limited by two vertical fractures. In the vicinity of the central injector and close to the surface, these fractures flatten out to form a tulip-shaped cone. In experiments A2 and A3, cones are more regular, while in experiment A4, they become bowl-shaped. For all experiments of series A, we measured the fracturing pressure λ_{fract}. All the fractures are initiated at supra-lithostatic pore pressure ($\lambda_{fract} > 1$). The measured values clearly show that the pressure required for fracturing the medium (λ_{fract}) is higher when the basal distributed fluid pressure λ_b is increased.

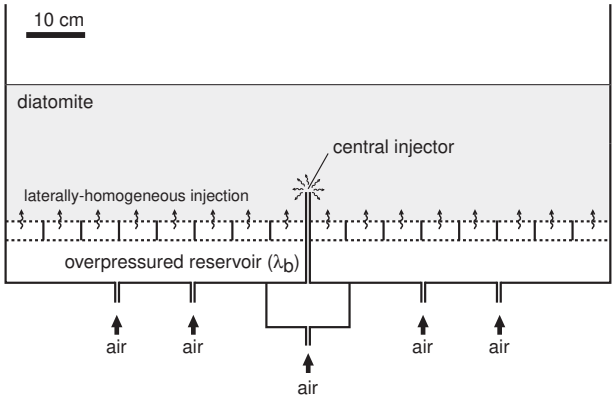

Fig. 2. Experimental Hele–Shaw cell (1 m long, 70 cm high and 2.5 cm thick). A reservoir of compressed air provides a basal constant pore pressure (λ_b). The fractures are initiated by injecting air through a 2-mm-wide central injector.

In series B, similar results are obtained. Cones are formed that become flattened at higher values of λ_b. Nevertheless, for experiment B1, a single fracture forms at the injector and propagates vertically. At a critical depth, this vertical fracture terminates and divides into two flat wings which form a V-shape. In all experiments of series B, the formation of cones corresponds to an uplift of the surface and the opening of tensile fractures at the top of the models.

In series C, the results of experiments C1 ($\lambda_b = 0$) and C2 ($\lambda_b = 0.3$) are similar to experiment B1, with a vertical fracture dividing into two flat wings. The depth of initiation of the V-shaped structure is greater in experiment C2 (14.8 cm for $\lambda_b = 0.3$) than in experiments C1 and B1 (11.2 cm and 9.1 cm, respectively, for $\lambda_b = 0$). In experiments C3 and C4, the cone is initiated at the central injector and is steeper than observed in experiments of the previous series conducted with the same λ_b. In experiment C4, the cone is flatter than in experiment C3, and many horizontal fractures are opened, probably caused by a high value of λ_b ($\lambda_b = 0.9$).

4. Discussion

4.1. Fracture pressure

The experiments of series A clearly show that the pore pressure required to initiate hydrofractures increases with λ_b. Similar results were obtained and discussed in a previous article by Mourgues et al. (2011). In the present study, we demonstrate that the failure pressure can be predicted by analytical solutions derived from Rozhko et al. (2007). The failure pressure at the centre of a localized source of pore pressure diffusing into a surrounding overburden is given by:

$$\lambda_{fract} = k + T/\left(\rho_{eff} g z\right) + \lambda_b(\beta_\sigma - \beta_\tau - k)/(\beta_\sigma - \beta_\tau) \quad (15)$$

where $k = \nu/(1-\nu)$

$$\beta_\sigma = 1 - 0.5\alpha[(1-2\nu)/(1-\nu)][1 - 1/(2\ln(4z/w))] \quad (16)$$

$$\beta_t = 0.25\alpha[(1-2\nu)/(1-\nu)][1/(\ln(4z/w))] \quad (17)$$

where w is the width of the source of pore pressure, z its depth and α the Biot coefficient. This analytical solution takes into account the coupling between pore-pressure and stresses caused by two different pore pressure fields (Fig. 4). The injection of air at the base of the model (λ_b) provides a laterally uniform pore-pressure field within the model that is responsible for a strong coupling between pore-pressure and stresses (Fig. 4a). As λ_b increases, the Mohr circle representing effective stresses shifts to the left and decreases in size according to an elastic envelope. When $\lambda_b = 1$, the Mohr circle reduces to a point centred at the origin. When λ_b exceeds 1, the stresses become tensile and the minimum principal stress becomes vertical, thus producing horizontal fractures (Cobbold and Rodrigues, 2007; Mourgues et al., 2011) in the case where:

$$\lambda_b = 1 + T/(\rho g z). \quad (18)$$

The stress inversion for $\lambda_b > 1$ is probably responsible for the opening of horizontal fractures in experiment A5 ($\lambda_b = 1$). The second

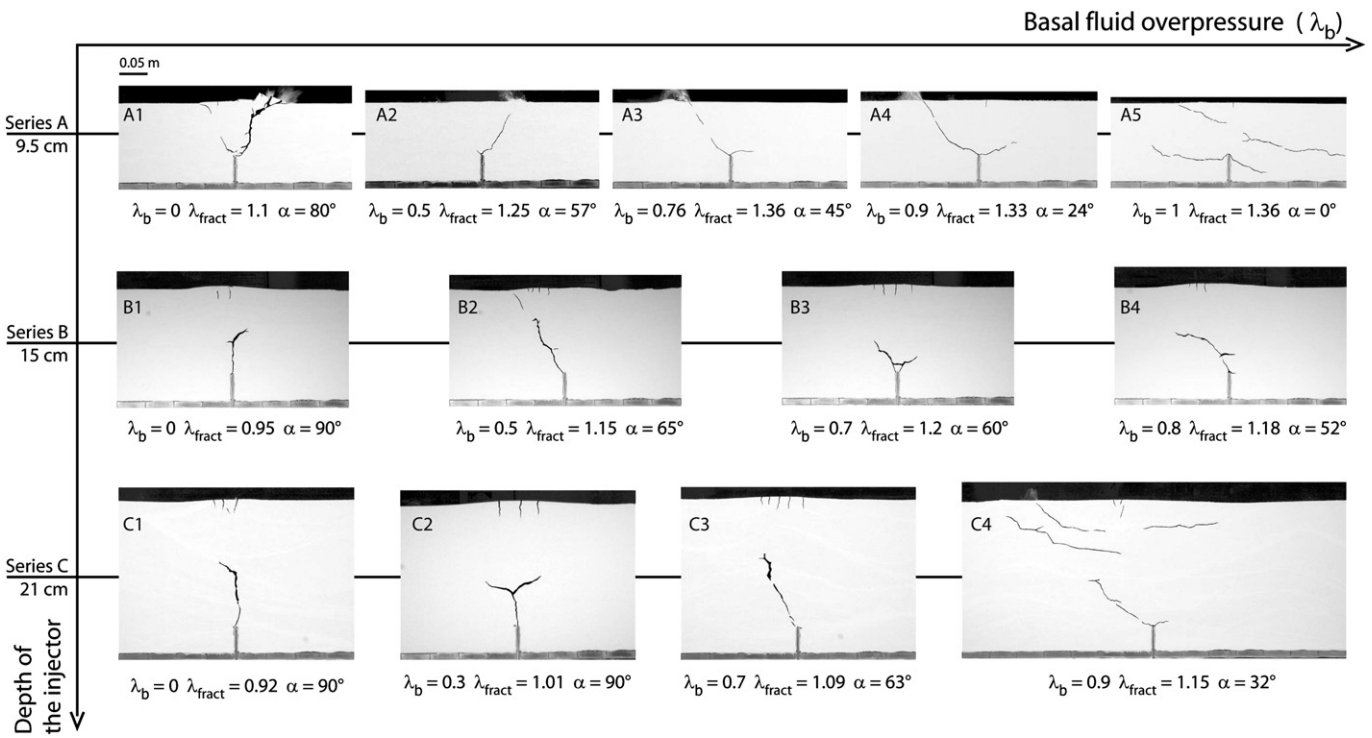

Fig. 3. Summary of experiments. The depth of the central injector is increased from 9.5 cm (row A), to 15 cm (row B) and 21 cm (row C). The pore fluid overpressure λ_b increases from left to right. λ_{fract} refers to the pore pressure required to initiate failure above the injector. For experiments involving a small basal fluid pressure and a thick cover (B1, C1 and C2), a fracture grows vertically before evolving into a V-shaped structure. In all other experiments (A1–A5, B2–B4, C3–C4), a V-shaped structure is initiated directly above the injector. We observe that all the wings flatten with increasing basal pore pressure λ_b.

injection of air at the central injector creates another pore pressure field that is superimposed on λ_b. The stress coupling caused by this injection is weaker than the previous injection, and the decrease in size of the Mohr circle is slower when pressure increases (Fig. 4b), so there is no stress inversion. As previously demonstrated by Mourgues et al. (2011), Fig. 4c shows a good correlation between the failure pressure predicted by Eq. (15) and the measurements of series A, where the silo effect was only moderate. As a consequence of pore pressure/stress coupling, the fluid pressure required to initiate hydraulic fracturing is higher than we might classically expect from relation $\sigma_3 + T$ with no stress coupling (Mourgues et al., 2011).

4.2. Pore pressure field and conical hydrofractures

In our experiments, vertical fractures only open in the thickest models (series B and C) with no basal pore fluid overpressure ($\lambda_b = 0$). In all the other models, two fractures open and form a V-shaped structure (cone). In Fig. 4d, the experimental results are plotted as a function of λ_b and lithostatic stress at the injector, together with the failure pressure predicted by Eq. (15) and the mean dip of the fractures. The dip is not always easy to evaluate because factures are sometimes curved. Hence, a mean dip is taken from measurements on the first 5 cm of fractures above the injector. Fig. 4d clearly shows that vertical fractures only appear for failure pressure (λ_{fract}) less than 1 (exp. B1, C1, C2). At $\lambda_{fract} > 1$, a cone is formed. We observe that the flattening of the cone may be correlated with the increase of λ_{fract}. When the fracture dips are plotted as a function of the fracturing pressure normalized to the vertical effective stress, $P_{fract}/\sigma_v' = \lambda_{fract}/(1-\lambda_b)$ (Fig. 5), we can see that the cones flatten with increasing $\lambda_{fract}/(1-\lambda_b)$ ratio. We then compare these results with numerical calculations of σ_1 trajectories that assume an elastic rheology and a steady-state pore-fluid pressure field. We plot the minimum dip (maximum deviation) of σ_1 at two different depths (normalized to the thickness) above the injector; the strong correlation with fracture dip demonstrates that the angle of the cone sides is controlled by stress rotation in the vicinity of the pressure source. This observation agrees with Anderson's calculation of stress rotation around a magma chamber and the formation of cone sheets (Anderson, 1936; Gudmundson, 2006). Contrary to Anderson's model or more modern analyses (Anderson, 1936; Gudmundson, 2006), which assume that magmatic pressure is confined within a chamber, the fluid overpressure in our experiment – or in a natural sand reservoir – diffuses into the surrounding overburden and creates a non-homogeneous pore pressure field. This non-hydrostatic pore-pressure field is responsible for stress rotation distant from the source (Fig. 6). Assuming that the permeability of the overburden is zero and that diffusion of pore-pressure does not occur, we can calculate the σ_1 orientation around a confined cylindrical pore pressure source (Fig. 6a). Calculations are performed here for an elastic rheology. As in Anderson's model, stress rotation occurs only in the vicinity of the pressurized chamber. When permeability is non-zero, a pore-pressure fluid-flow propagates around the cylindrical reservoir. The pressures are calculated for steady-state fluid flow. This pore-pressure field is responsible for additional forces (seepage forces) applied to the porous medium, which lead to stress rotation (Mourgues and Cobbold, 2003). A more pronounced stress rotation is observed far from the reservoir in the permeable case than in the case where the overburden is impermeable (Fig. 6a). This phenomenon may be a significant factor influencing the formation of non-vertical hydrofractures and conical intrusions in sedimentary basins. The reader should bear in mind that seepage forces depend only on the pore-pressure field and not on the pore-fluid velocity (Mourgues and Cobbold, 2003). For the same pressure field, the seepage forces are the same in high- and low-permeability strata. A significant difference may arise because of the pressure diffusion time (Eq. (15)); in low-permeability strata (around 10^{-19} m^2 darcy), the pressure front will diffuse 250 m in less than 250,000 years. If a sand body is initially overpressured for a long period (during its burial) before a triggering event, the geometry of the intrusion will be significantly modified by the pore-pressure field. This contrasts with models of magmatic chambers in which the

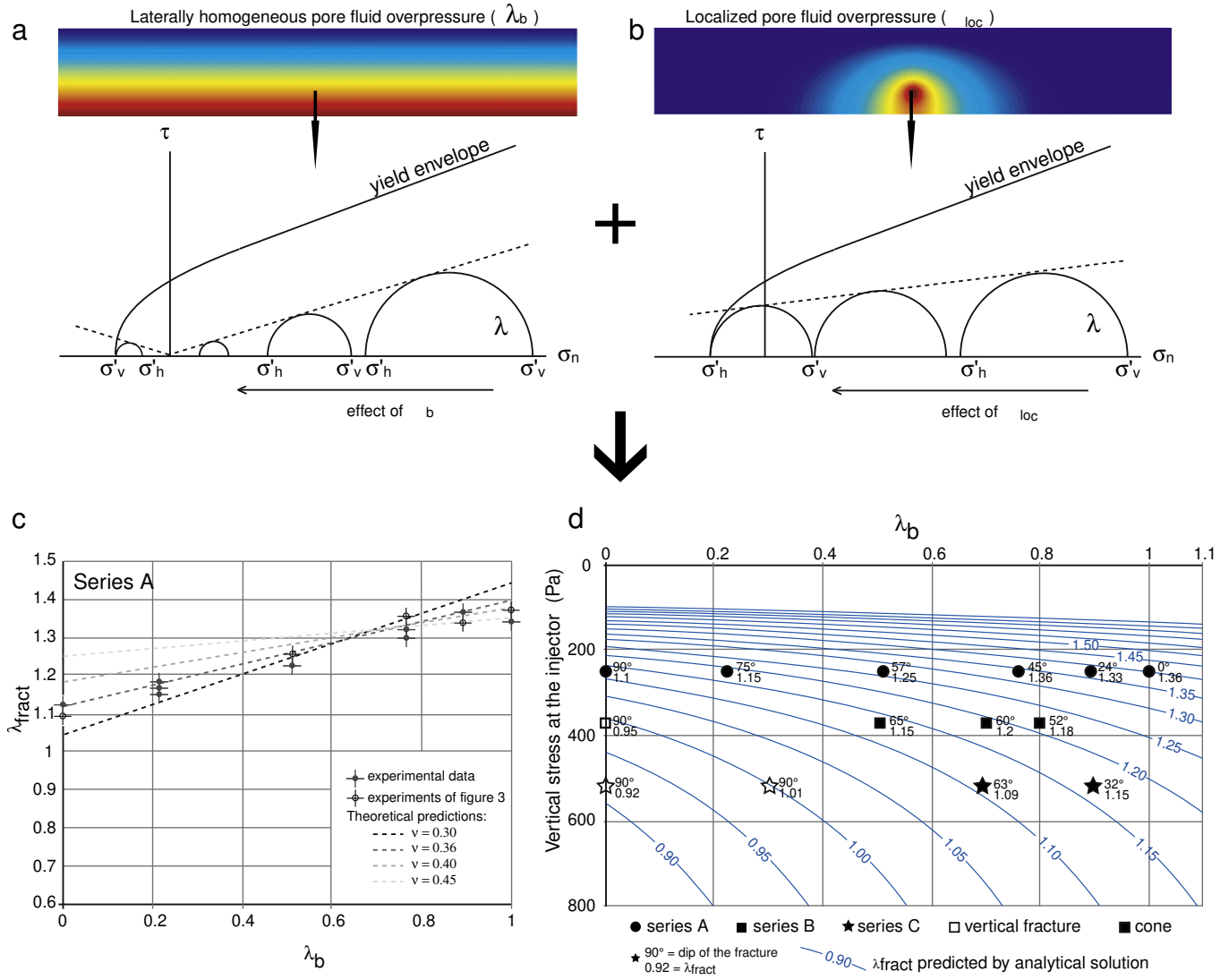

Fig. 4. a: The injection of air at the base of the model (λ_b) provides a laterally uniform pore-pressure leading to strong coupling between pore-pressure and stresses (Mourgues et al., 2011). b: The pore pressure field around a central injection is associated with a weaker coupling between pore pressure and stresses. c–d: The combination of these two stress fields is used to estimate theoretically the pore-pressure required to initiate hydrofractures. Panel c shows the good correlation between the results of series-A experiments (see Fig. 3) and the theoretical predictions. All the experimental results (λ_{fract}, fracture dips) and theoretical predictions (blue lines) are plotted in panel d. Empty symbols correspond to a single vertical fracture observed on top of the injector, solid symbols to the formation of an apical cone.

magmatic pressure remains confined within the reservoir (i.e. the magma chamber). Nevertheless, this phenomenon may also occur when magma intrudes sedimentary sequences. Certain authors (Jamtveit et al., 2004) have calculated the pore-fluid overpressure generated by heating of water around a magmatic intrusion. Under extreme conditions, if the pore-fluid overpressure is sufficiently high, hydrothermal vents will form (Svensen et al., 2004; Svensen et al., 2007). However, if the conditions required for hydrothermal venting are not reached, we can assume that the pore overpressure may influence the vertical propagation of the dykes by modifying the stress field around the intrusion.

Formation of a cone and its flattening are favoured by high values of parameter $\lambda_{fract}/(1-\lambda_b)$ (Fig. 5). Because λ_{fract} increases with T and with the decreasing z, a consolidated sedimentary cover may facilitate the formation of a cone near the surface. Moreover, the presence of fluid overpressure already distributed in the sediment (for example, due to compaction disequilibrium) may increase the depth at which cones form, and may favour the development of flatter cones. In the sand injectite analogue experiments carried out by Rodrigues et al. (2009), the intruded sedimentary cover was highly overpressured (Fig. 7 in Rodrigues et al., 2009), and only flat conical intrusions were formed. Our present study supports their findings and is in agreement with the results of Gressier et al. (2010) on magmatic intrusions. These latter authors demonstrated analytically and experimentally that pore fluid overpressure within strata increases the dyke-to-sill transition depth.

4.3. Transition between vertical and inclined fractures

In experiments B1, C1 and C2, hydraulic fractures initially propagate vertically before dividing into two branches that form a V-shaped structure. The cones are initiated at depths of 9.1 cm and 11.2 cm for experiments B1 and C1, where $\lambda_b = 0$. In experiment C2, where the distributed fluid overpressure λ_b is 0.3, this depth reaches 14.8 cm. This result is in agreement with Fig. 5, which indicates that the formation of inclined fractures is favoured by low effective stresses

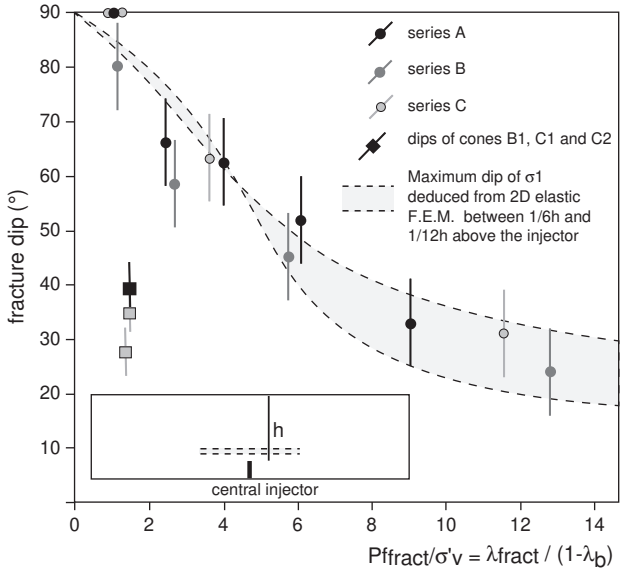

Fig. 5. Observed fracture dips plotted as a function of normalized failure pressure. The fractures flatten with increasing $\lambda_{fract}/(1-\lambda_b)$. We compare these results with numerical calculations of σ_1 dips assuming an elastic rheology and a steady-state pore pressure. The dashed lines represent the maximum σ_1 dips calculated at height $h/6$ and $h/12$ above the injector (h = depth of the central injector). The angle of the cone is controlled by the stress rotation in the vicinity of the pressure source, in agreement with Anderson's model (Anderson, 1936). In experiments B1, C1 and C2, where a vertical fracture is initially formed, the cone is flatter than predicted from elastic rheology. The plastic deformation taking place during fracture growth and the dynamic evolution of pore-pressure around the fracture may explain this behaviour.

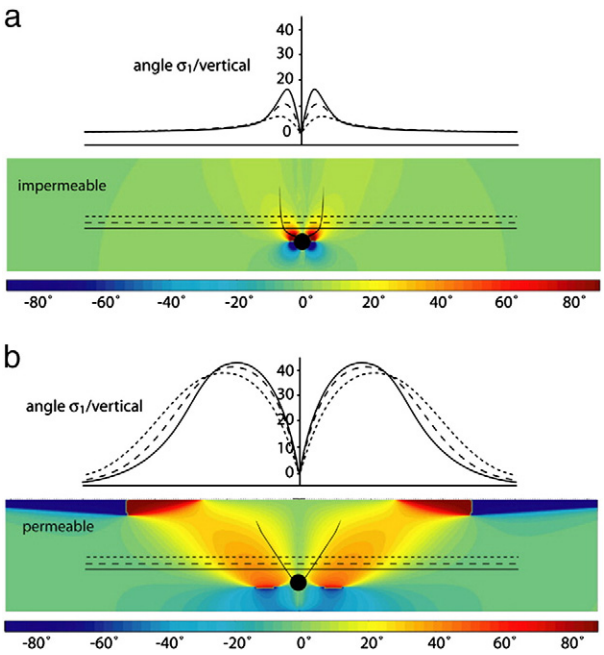

Fig. 6. Comparison between stress rotations and shapes of mode-1 hydrofractures around a cylindrical source of pore pressure ($\lambda = 1.2$). We assume that the conditions are steady state. In panel (a), the excess pore-pressure is confined within the cylinder. The overburden is impermeable, stress rotations are localized close to the source and fractures become rapidly vertical. In panel (b), the overburden is permeable and the excess pore-pressure diffuses away from the source. Stress rotations occur far from the source, leading to a large V-shaped fracture.

or high distributed fluid overpressures. Nevertheless, by plotting the dips of cones B1, C1 and C2 (see Fig. 5), we observe that these cones are flatter than those formed at the central injector. Moreover, the dips are gentler than predicted by the elastic model of σ_1 trajectories. Two reasons may explain this difference. Firstly, σ_1 orientation is calculated elastically (such as in gelatine), in contrast to the propagation of hydraulic fractures in cohesive powders in which plastic deformation prevails. Moreover, the fractures propagate in less than 0.5 s through the model, which is close to the pressure diffusion time ($t_o = 400$ ms). Thus, we can assume that the steady-state approximation for fluid flow becomes invalid as soon as the fracture starts to propagate. This may be also the case for clastic intrusions.

To improve our understanding of the transition between the vertical feeder dyke and V-shaped structures near the free surface, we measured the deformation in an experiment similar to C1. Particle Imaging Velocimetry was used with a 5-pixels correlation window (Adam et al., 2005), and some of the results are presented in Fig. 7. All the particle displacements are larger than 75 μm, which is more than the maximum displacement caused by elastic deformation (≈ 5 μm), so we infer that the deformation recorded by PIV is attributable to plasticity. During the vertical growth of the fracture (Fig. 7a), we clearly observe a cone of vertical upward displacements just above the tip of the dyke. These vertical displacements are responsible for a small uplift of the surface, and accelerate as the fracture rises (Fig. 7b). Two large shear bands limit the cone. The symmetry of shear deformation at the tip indicates that the fracture opens exclusively in pure tension mode. In Fig. 7b–c, we observe two branches dipping at 40°, which are similar in appearance to experimentally-produced analogues of magmatic intrusions (Mathieu et al., 2008). These latter authors attributed the formation of such structures to the presence of conjugate normal faults dipping towards the intrusion. These normal faults and tension fractures are predicted from elastic analytical solutions (Koide and Bhattacharji, 1975). According to several authors (Donnadieu and Merle, 1998; Mastin and Pollard, 1988; Mathieu et al., 2008; Weertman, 1980), the fracturing fluid is channelled by normal faults at the tip of dyke, and infiltration results in the formation of two branches; our experiments do not support such a phenomenon. As soon as the hydrofracture starts to propagate vertically, large reverse shear bands are recorded rather than normal faults. The inclined fracture does not follow the shear bands that develop with a steeper angle (Fig. 7c), so we assume that infiltration of fluids into a dilating shear band is not the mechanism responsible for the formation of inclined sheets. To explain the formation of conical intrusions, Cartwright et al. (2008) proposed the formation of small cupola-shaped laccoliths of sand at the top of a feeder dyke, which provided the required stress conditions according to the magma chamber model. In our experiments, no laccolith is formed before the growth of the V-shaped structure (Fig. 8). At the tip of the opening inclined fracture, a small zone (1 to 2 cm long) of stronger shear deformation is observed with the same dip as the fracture (Fig. 7c–d). We attribute this shear deformation to a mixed mode (tension and shear) fracture growth. In a second stage (Fig. 7e–f), we observe that shear deformation defining the cone of vertical displacement is localized into two fine shear bands that accelerate the surface uplift. At this

Fig. 7 Different stages of fracture growth (case C1). Pictures are analysed by P.I.V. technique. Vertical displacements and shear deformations are calculated between two successive pictures (frame rate: 100 fps). The correlation window is 5 pixels wide. During its vertical propagation (a–b), the fracture opens purely in tension. A cone of vertical upward displacement is observed just above the tip of the dyke. This vertical displacement is responsible for a small uplift of the surface that accelerates as the fracture rises (b). In panels b–c–d, we observe the formation of two inclined wings, dipping at about 40°. These fractures open in mixed modes because they do not follow the large shear bands that develop with a steeper angle. In panel (e), the shear deformation is localized along narrow shear bands that channel the percolation of fluids towards the surface.

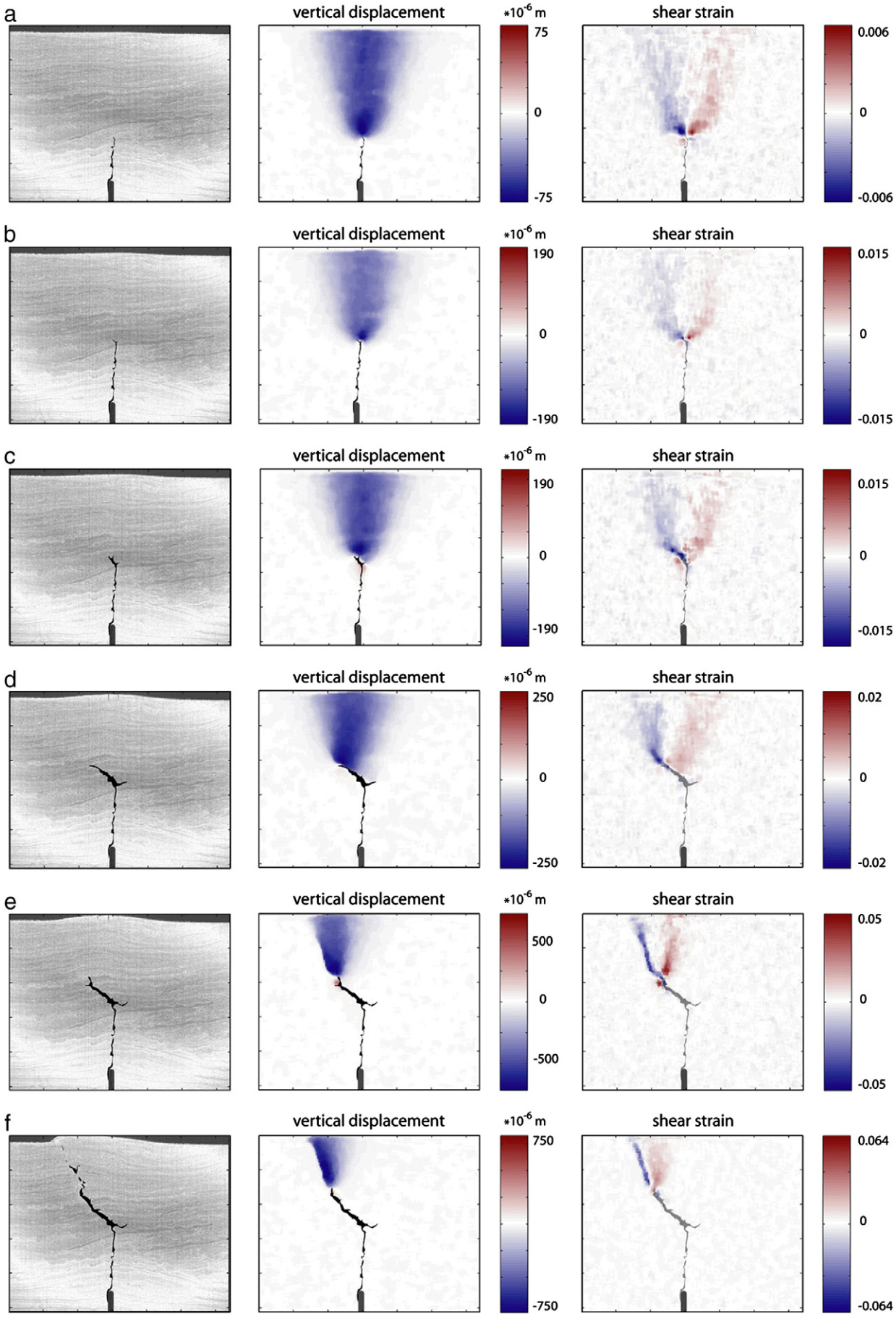
a
vertical displacement
*10^-6 m
75
0
-75
shear strain
0.006
0
-0.006
b
vertical displacement
*10^-6 m
190
0
-190
shear strain
0.015
0
-0.015
c
vertical displacement
*10^-6 m
190
0
-190
shear strain
0.015
0
-0.015
d
vertical displacement
*10^-6 m
250
0
-250
shear strain
0.02
0
-0.02
e
vertical displacement
*10^-6 m
500
0
-500
shear strain
0.05
0
-0.05
f
vertical displacement
*10^-6 m
750
-750
shear strain
0.064
0
-0.064

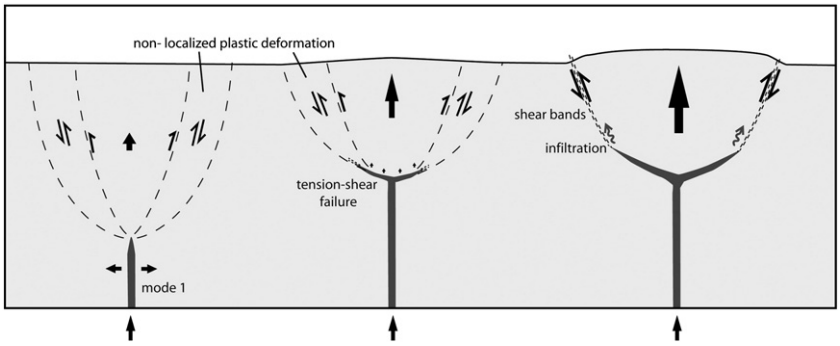

Fig. 8. Schematic diagram illustrating the formation mechanism of V-shaped fractures at the top of a feeder dyke as observed in our experiments. At first, a mode-1 fracture grows vertically. During this stage, two large bands of plastic shear deformation define a cone with small vertical displacement. At a critical depth, the fracture separates into two branches, which continue to open in tension but with an additional component of shear. In the final stage, the fluid percolates the two well developed shear bands to reach the surface.

stage, opening of the fracture seems to be hindered, and only two disconnected zones of high dilatancy are observed, indicating that fluid infiltrates the shear bands without opening any hydraulic fractures.

4.4. Comparison with the tripartite architecture of the Panoche Giant Injection Complex

The Panoche Giant Injection Complex (Hurst et al., 2011; Vigorito and Hurst, 2010; Vigorito et al., 2008) is the largest and best exposed analogue for regionally developed sand injectites, (San Joaquim valley (California)). Recent detailed observations (Vigorito and Hurst, 2010) suggest a common tripartite architecture of the injection complex, which is recognized in three distinctive geographical sectors: the lower dyke zone, the sill zone and the upper dyke zone (Fig. 9). The lower dyke zone is identified in the parent unit belt (PUB), where channel complexes form the parent units and probably also the pressure cell (where the pore pressure attains values close to lithostatic) required for sand injection. Sparse high-angle dykes, which are up to 6 m wide and 600 m long, emanate from the basal unit of PUB. The upper part of the PUB contains extensively deformed sandstones which feed dykes, and both dykes and sills higher in the section. The sill zone makes up a restricted stratigraphic interval in the intrusive belt (IB). This zone is mainly characterized by sills and large (8–12 m aperture) low-angle dykes (with random strike distribution) that can cross-cut up to 230 m of host strata. The upper part of the intrusive belt is dominated by the upper dyke zone characterized by high-angle and bifurcating dykes that become thinner and more abundant upward. Locally, these dykes terminate below what is interpreted as a sand extrudite. The basal contact of this extruded formation is reported to be irregular, being characterized by depressions interpreted as paleo-pockmarks and local metre-scale sandstone volcanoes.

Bearing in mind these observations, we can draw a parallel (Fig. 9) with the results of experiments B1, C1 and C2. In all these experiments, a tripartite architecture can also be clearly identified: i) a basal vertical dyke, ii) a zone where flat inclined fractures are opened and enlarged, which can be interpreted as equivalent to the sill zone where randomly-oriented low-angle dykes are reported and iii) an

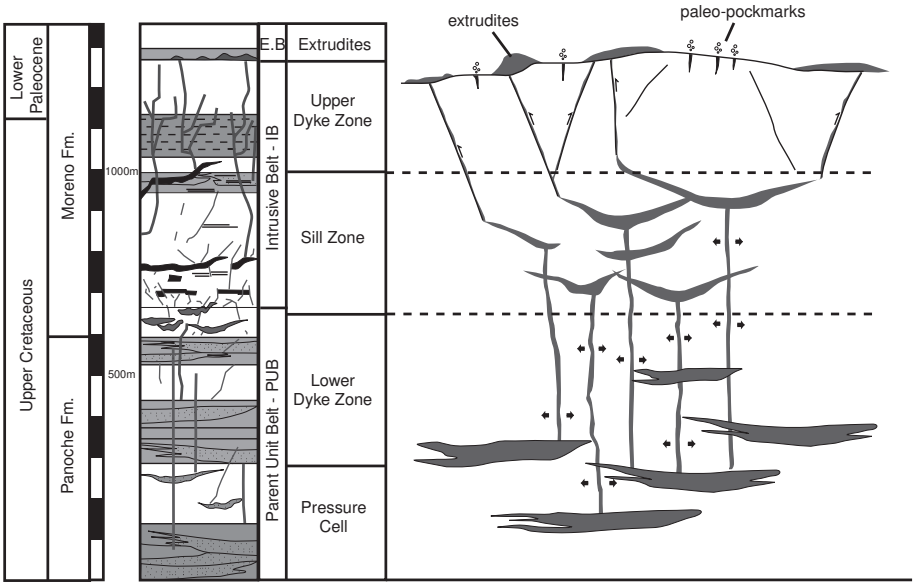

Fig. 9. Schematic cross-section of the northern sector of the Panoche Giant Injectite Complex (PGIC). The sill zone observed in the PGIC is consistent with the formation of flat cones in the experiments. The dykes observed in the lower dyke zone probably feed the sill zone and are opened in a pure tension regime (mode 1). The formation of dykes in the upper zone is assumed to result from deformation of the cover induced by the growth of sills. These dykes may follow initial shear bands and tensile fractures developed during deformation of the free surface. The formation of tensile fractures disconnected from injectite networks may provide preferential pathways for fluids and lead to the formation of pockmarks.

upper zone characterized by steep fractures that open following shear deformation caused by the growth of the sills. In this upper zone, shear bands initially develop before the injection of fluids. The resulting fractures are thinner than those opened in mode 1 in the basal dyke zone. This is in agreement with the observations of the Panoche complex, although no shear deformation is clearly identified. Vigorito and Hurst (2010) also reported that the dykes in the upper zone become more abundant upward. This may be due to the development of tensile stresses and the opening of tension fractures in response to the uplift of the free surface. The occurrence of paleo-pockmarks in the extrudite is also consistent with the formation of tension fractures. These fractures may favour the expulsion of fluids without being connected to the sand injection complex. The irregularity observed at the basal contact of the extruded formation may also be compatible with the deformation of the surface induced by the emplacement of sandstone intrusions at depth.

5. Conclusion

In this study, physical experiments of hydraulic fracturing are carried out to determine the effects of pore-fluid overpressure and plastic deformation on the formation of vertical and conical structures in sedimentary basins. We demonstrate that the pore pressure field generated around an overpressured parent body may be responsible for a pore-pressure/stress coupling that can favour high fracture pressure and stress rotation leading to the formation of inclined sheet-like fractures. Inclined fractures are initiated at the source when the required supralithostatic fracture pressure is attained in consolidated sediments at shallow depth or in overburden subjected to high pore-fluid overpressure. At lower fracture pressure, a tripartite injection-architecture is obtained. Only a single fracture is found to open in mode 1, which then grows vertically until a critical depth is attained when it splits into two branches open in mixed modes. The formation of inclined fractures leads to an uplift of the free surface, along with the development of shear bands and tensile fractures that provide conduits for fluids. The final morphology of the fracture network is very similar to the common tripartite architecture of various injection complexes, indicating that different mechanisms are involved in the formation of dykes under and above the sill zone. Such results may be significant in the understanding of fluid migration pathways through sandstone intrusion complexes.

Acknowledgements

This study was supported by grants from Region Pays de la Loire, France. We thank two anonymous reviewers and editor Yanick Ricard for their useful comments. We also thank Ian Harris for reading and editing the article.

References

Adam, J., Urai, J.L., Wieneke, B., Oncken, O., Pfeiffer, K., Kukowski, N., Lohrmann, J., Hoth, S., van der Zee, W., Schmatz, J., 2005. Shear localisation and strain distribution during tectonic faulting—new insights from granular-flow experiments and high-resolution optical image correlation techniques. J. Struct. Geol. 27, 283–301.
Anderson, E.M., 1936. The dynamics of formation of cone sheets, ring dykes and cauldron subsidences. Proc. R. Soc. Edinb. 56.
Cartwright, J., 2007. The impact of 3D seismic data on the understanding of compaction, fluid flow and diagenesis in sedimentary basins. J. Geol. Soc. Lond. 164, 881–893.
Cartwright, J., 2010. Regionally extensive emplacement of sandstone intrusions: a brief review. Basin Res.. doi:10.1111/j.1365-2117.2009.00455.x (v.).
Cartwright, J., James, D., Huuse, M., Vetel, W., Hurst, A., 2008. The geometry and emplacement of conical sandstone intrusions. J. Struct. Geol. 30, 854–867.
Chang, H., 2004, Hydraulic fracturing in particulate materials, Georgia Institute of Technology, phD thesis.
Cobbold, P.R., Castro, L., 1999. Fluid pressure and effective stress in sandbox models. Tectonophysics 301, 1–19.
Cobbold, P.R., Rodrigues, N., 2007. Seepage forces, important factors in the formation of horizontal hydraulic fractures and bedding parallel fibrous veins ('beef' and 'cone-in-cone'). Geofluids 7, 313–322.
Davies, R., 2003. Kilometer-scale fluidization structures formed during early burial of a deep-water slope channel on the Niger Delta. Geology 31, 949–952.
Davis, D., Suppe, J., Dahlen, F.A., 1983. Mechanics of fold-and-thrust belts and accretionary wedges. J. Geophys. Res. 88, 1153–1172.
De Boer, W., Rawlinson, P.B., Hurst, A., 2007. Successful exploration of a sand injectite complex: Hamsun prospect, Norway Block 24/9. In: Hurst, A., Cartwright, J. (Eds.), Sand Injectites: Implications for Hydrocarbon Exploration and Production: AAPG Memoir, 87, pp. 65–68.
Donnadieu, F., Merle, O., 1998. Experiments on the indentation process during cryptodome intrusions: new insights into Mount St. Helens deformation. Geology 26, 79–82.
Duranti, D., 2007. Large-scale sand injection in the Paleogene of the North Sea: modeling of energy and flow velocities. In: Hurst, A., Cartwright, J. (Eds.), Sand Injectites: Implications for Hydrocarbon Exploration: AAPG Memoir, 87, pp. 129–139.
Duranti, D., Hurst, A., Bell, C., Groves, S., Hanson, R., 2002. Injected and remobilised Eocene sandstones from the Alba Field, UKCS: core and wireline characteristics. Pet. Geosci. 8, 99–107.
Fialko, Y., Khazan, Y., Simon, M., 2001. Deformation due to a pressurized horizontal circular crack in an elastic half space, with applications to volcano geodesy. Geophys. J. Int. 146, 181–190.
Galland, O., Planke, S., Neumann, E.R., Malthe-Sorenssen, A., 2009. Experimental modelling of shallow magma emplacement: application to saucer-shaped intrusions. Earth Planet. Sci. Lett. 277, 373–383.
Goulty, N., Schofield, N., 2008. Implications of simple flexure theory for the formation of saucer-shaped sills. J. Struct. Geol. 30, 812–815.
Gressier, J.B., Mourgues, R., Bodet, L., Mathieu, J.Y., Galland, O., Cobbold, P.R., 2010. Control of pore fluid pressure on depth of emplacement of magmatic sills: an experimental approach. Tectonophysics 489, 1–13.
Gudmundson, A., 2006. How local stresses control magma-chamber ruptures, dyke injections, and eruptions in composite volcanoes. Earth Sci. Rev. 79, 1–31.
Gudmundsson, A., 1990. Magma chambers modeled as cavities explain the formation of rift zone central volcanoes and their eruption at divergent plate boundaries. Tectonophysics 176, 257–275.
Hansen, D.M., Cartwright, J.A., 2006a. The three-dimensional geometry and growth of forced folds above saucer-shaped igneous sills. J. Struct. Geol. 28, 1520–1535.
Hansen, D.M., Cartwright, J.A., 2006b. Saucer-shaped sill with lobate morphology revealed by 3D seismic data: implications for resolving a shallow-level sill emplacement mechanism. J. Geol. Soc. Lond. 163.
Horsrud, P., Sonstebo, E.F., Boe, R., 1998. Mechanical and petrophysical properties of North Sea shales. Int. J. Rock Min. Sci. 35, 1009–1020.
Hubbert, M.K., 1937. Theory of scale models as applied to the study of geologic structures. Geol. Soc. Am. Bull. 48, 1459–1520.
Hubbert, M.K., Willis, D.G., 1957. Mechanics of hydraulic fracturing. AIME 210, 153–166.
Hurst, A., Cartwright, J., 2007. Sand injectite: implications for hydrocarbon exploration and production. AAPG Mem. 87.
Hurst, A., Cartwright, J.A., Huuse, M., Jonk, R., Schwab, A.M., Duranti, D., Cronin, B.T., 2003. Significance of large-scale sand injectites as long-term fluid conduits: evidence from seismic data. Geofluids 3, 263–274.
Hurst, A., Scott, A., Vigorito, M., 2011. Physical characteristics of sand injectites. Earth-Sci. Rev. 106, 215–246.
Huuse, M., Mickelson, M., 2004. Eocene sandstone intrusions in the Tampen Spur area (Norwegian North Sea Quad 34) imaged by 3D seismic data. Mar. Pet. Geol. 21, 141–155.
Huuse, M., Cartwright, J., Gras, R., Hurst, A., 2005. Km-scale sandstone intrusions in the Eocene of the Outer Moray Firth (UK North Sea): migration paths, reservoirs, and potential drilling hazards. Petroleum Geology of NW Europe: Proceedings of the 6th Conference, pp. 1577–1594.
Jaeger, J.C., Cook, N.G.W., 1969. Fundamentals of Rock Mechanics. Barnes and Nobles, New York. (513 pp.).
Jamtveit, B., Svensen, H., Podladchikov, Y.Y., Planke, S., 2004. Hydrothermal vent complexes associated with sill intrusions in sedimentary basins. Bull. Geol. Soc. Lond. 234, 233–241.
Janssen, H.A., 1895. Versuche uber getreidedruck in Silozellen. Z. Ver. Dtsch. Ing. 39, 1045–1049.
Jenkins, O.P., 1930. Sandstone dikes as conduits for oil migration through shales. AAPG Bull. 14, 411–421.
Kavanagh, J.L., Menand, T., Sparks, R.S.J., 2006. An experimental investigation of sill formation and propagation in layered elastic media. Earth Planet. Sci. Lett. 245, 799–813.
Koide, H., Bhattacharji, S., 1975. Formation of fractures around magmatic intrusions and their role in ore localization. Econ. Geol. 70, 781–799.
Lothe, A.E., Borge, H., Gabrielsen, H., 2004. Modelling of hydraulic leakage by pressure and stress simulations and implications for Biot's constant: an example from Halten Terrace, offshore Mid-Norway. Pet. Geosci. 10, 199–213.
Malthe-Sorenssen, A., Planke, S., Svensen, H., Jamtveit, B., 2004. Formation of saucer-shaped sills. In: Breitkreuz, C., Petford, N. (Eds.), Physical Geology of High-level Magmatic Systems: London, Geol. Soc. Lond. Spec. Pub, pp. 215–227.
Mastin, L.G., Pollard, D.D., 1988. Surface deformation and shallow dike intrusion processes at Inyo Craters, Long Valley, California. J. Geophys. Res. 93, 13221–13235.
Mathieu, L., van Wyk de Vries, B., Holohan, E.P., Troll, V.R., 2008. Dykes, cups, saucers and sills: analogue experiments on magma intrusion into brittle rocks. Earth Planet. Sci. Lett. 271, 1–13.
Menand, T., 2008. The mechanics and dynamics of sills in layered elastic rocks and their implications for the growth of laccoliths and other igneous complexes. Earth Planet. Sci. Lett. 267, 93–99.
Mogi, K., 1958. Relations between eruptions of various volcanoes and the deformations of the ground surfaces around them. Res. Inst. Univ. Tokyo 36, 99–134.
Mourgues, R., Cobbold, P.R., 2003. Some tectonic consequences of fluid overpressures and seepage forces as demonstrated by sandbox modelling. Tectonophysics 376, 75–97.

Mourgues, R., Cobbold, P.R., 2006a. Sandbox experiments on gravitational spreading and gliding in the presence of fluid overpressures. J. Struct. Geol. 28, 887–906.
Mourgues, R., Cobbold, P.R., 2006b. Thrust wedges and fluid overpressures: sandbox models involving pore fluids. J. Geophys. Res. 111.
Mourgues, R., Lecomte, E., Vendeville, B., Raillard, S., 2009. An experimental investigation of gravity-driven shale tectonics in progradational delta. Tectonophysics 474, 643–656.
Mourgues, R., J. B. Gressier, L. Bodet, D. Bureau, and A.Gay, 2011, "Basin scale" versus "localized" pore pressure / stress coupling — implications for trap integrity evaluation: Marine and Petroleum Geology, v.under publication.
Murdoch, L.C., 1992. Hydraulic fracturing of soil during laboratory experiments. Part 1: methods and observations. Geotechnique 43, 255–265.
Murdoch, L.C., 2002. Mechanical analysis of idealized shallow hydraulic fracture. J. Geotech. Env. Eng. 128, 488–495.
Murdoch, L.C., Slack, W., 2002. Forms of hydraulic fractures in shallow fine-grained formations. J. Geotech. Env. Eng. 128, 479–487.
Pollard, D.D., 1973. Derivation and evolution of a mechanical model for sheet intrusions. Tectonophysics 19, 233–269.
Pollard, D.D., Holzhausen, G., 1979. On the mechanical interaction between a fluid-filled fracture and the Earth's surface. Tectonophysics 53, 27–57.
Pollard, D.D., Johnson, A.M., 1973. Mechanics of growth of some laccolith intrusions in the Henry Mountains, Utah. Part II. Tectonophysics 18, 311–354.
Polteau, S., Mazzini, A., Galland, O., Planke, S., Malthe-Sorenssen, A., 2008. Saucer-shaped intrusions: occurrences, emplacement and implications. Earth Planet. Sci. Lett. 266, 195–204.
Price, N.J., Cosgrove, J.W., 1990. Analysis of Geological Structures. Cambridge University Press, N.Y.502 pp.
Ramberg, H., 1981. Gravity, Deformation and the Earth's Crust: N.Y. (452 pp. p.).
Rodrigues, N., Cobbold, P.R., Løseth, H., 2009. Physical modelling of sand injectites. Tectonophysics 474, 610–632.
Rozhko, A.Y., Podladchikov, Y.Y., Renard, F., 2007. Failure patterns caused by localized rise in pore-fluid overpressure and effective strength of rocks. Geophys. Res. Lett. 34. doi:10.1029/2007GL031696 (p.).
Schwartz, H., Sample, S., Werberling, K.D., Minisini, D., Moore, C., 2003. An ancient linked fluid migration system: cold-seep deposits and sandstone intrusions in the Panoche Hills, California, USA. Geo-Mar. Lett. 23, 340–350.
Shoulders, S., Cartwright, J.A., 2004. Constraining the depth and timing of large-scale conical sandstone intrusions. Geology 32, 661–665.
Shoulders, S., Cartwright, J.A., Huuse, M., 2007. Large-scale conical sandstone intrusions and polygonal fault systems in Tranche 6, Faroe–Shetland Basin. Mar. Pet. Geol. 24, 173–188.
Surlyk, F., Gjelberg, J., Noe-Nygaard, N., 2007. The Upper Jurassic Harleev Formation of East Greenland: a giant sedimentary injection complex. In: Hurst, A., Cartwright, J. (Eds.), Sand Injectites: Implications for Hydrocarbon Exploration and Production: AAPG Memoir, 87, pp. 141–150.
Svensen, H., Planke, S., Malthe-Sorenssen, A., Jamtveit, B., Myklebust, R., Eldem, T.R., Rey, S.S., 2004. Release of methane from a volcanic basin as a mechanism for initial Eocene global warming. Nature 429, 542–545.
Svensen, H., Planke, S., Chevallier, L., Malthe-Sorenssen, A., Corfu, F., Jamtveit, B., 2007. Hydrothermal venting of greenhouse gases triggering Early Jurassic global warming. Earth Planet. Sci. Lett. 256, 554–566.
Takada, A., 1990. Experimental study of propagation of liquid-filled crack in gelatin: shape and velocity in hydrostatic stress condition. J.G.R. 95, 8471–8481.
Thompson, K., Schofield, N., 2008. Lithological and structural controls on the emplacement and morphology of sills in sedimentary basins. Structure and Emplacement of High-Level Magmatic Systems: Geol Soc Spec Publication, 302, pp. 31–44.
Thomson, K., Hutton, D., 2004. Geometry and growth of sill complexes: insights using 3D seismic from the North Rockall Trough. Bull. Volcanol. 66, 364–375.
Vigorito, M., Hurst, A., 2010. Regional sand injectite architecture as a record of pore-pressure evolution and sand redistribution in the shallow crust: insights from the Panoche Giant Injection Complex, California. J. Geol. Soc. Lond. 167, 889–904.
Vigorito, M., Hurst, A., Cartwright, J., Scott, A., 2008. Regional-scale subsurface sand remobilization: geometry and architecture. J. Geol. Soc. Lond. 165, 609–612.
Weertman, J., 1980. The stopping of a rising, liquid-filled crack in the earth's crust by a freely slipping horizontal joint. J. Geophys. Res. 85, 967–976.